Enhancing the Hydrogen Evolution Reaction on Ru/KTN through an $RuCl_X$ Intermediate Strategy

Guangzhen Zhao,[a,b] Chengzhi Xiao,[b] Tongzhou Hong,[b] Guoliang Gao,*[b] Guang Zhu,*[b]

[a] State Key Laboratory of Biobased Material and Green Papermaking, Qilu University of Technology, Jinan, 250353, China

[b] Key Laboratory of Spin Electron and Nanomaterials of Anhui Higher Education Institutes, Suzhou University, Suzhou, 234000, China

1. Experimental sections

1.1 Materials and Chemicals

Material: Ti_2AlN (500 mesh) was purchased from FoShan XinXi Technology Co., Ltd. Commercial $RuCl_3$ was obtained from Sigma-Aldrich. KOH was obtained from Sinopharm Group Co., Ltd. Commercial 20 wt.% Pt/C was acquired from Macklin Chemical Reagent Co., Ltd.

1.2. Synthesis of KTN

Add 1 g of Ti_2AlN (500 mesh) to 150 mL of 5 M KOH solution and stir the mixture for 30 minutes to form a suspension. Then transfer it to a Teflon-lined hydrothermal reactor and maintain it at 150 °C for 12 hours. After the reaction, separate the resulting solid, wash it six times with deionized water, and dry it at 60 °C to obtain a gray solid sample. This sample is a composite of $K_2Ti_8O_{17}$ and partially remaining Ti_2AlN, labeled as KTN.

1.3. Synthesis of Ru/KTN-Air

Dissolve 0.5 g of $RuCl_3$ in 50 mL of deionized water and stir for 30 minutes. Then, add 0.5 g of the previously mentioned KTN, sonicate the mixture for 30 minutes, and stir for an additional 12 hours. Afterward, dry the mixture in an air-circulating oven at 80 °C to obtain $RuCl_3$/KTN powder samples. The resulting $RuCl_3$/KTN samples are placed in a muffle furnace and heated at a rate of 2 °C min^{-1} to 200 °C, where they are annealed for 2 hours, yielding Ru/KTN-Air. To investigate the effect of the oxidation process on the structure of $RuCl_3$, commercial $RuCl_3$ was placed in a muffle furnace and subjected to the same sintering procedure, resulting in $RuCl_x$ samples.

1.4. Synthesis of Ru/KTN-T

Place the Ru/KTN-Air sample in a tube furnace under a flowing hydrogen and argon atmosphere (5% H_2 / 95% Ar). Heat at a rate of 2 °C min^{-1} to 300 °C and maintain for 2 hours of annealing to obtain the Ru/KTN-T samples. To investigate the effect of temperature on the catalyst, $RuCl_3$/KTN powder is placed in a tube furnace under the same flowing hydrogen and argon atmosphere (5% H_2 / 95% Ar) and heated at 2 °C min^{-1} to 200 °C, 300 °C, and 400 °C for 2 hours of annealing, producing comparison samples Ru/KTN-200, Ru/KTN-300, and Ru/KTN-400.

2. Characterization

X-ray powder diffraction (XRD) patterns were obtained using a Smart Lab 3KW diffractometer. Transmission electron microscopy (TEM) was performed on a Tecnai G2 F20. X-ray photoelectron spectroscopy (XPS, Thermo Escalab 250Xi) was conducted to identify the valence states of the elements. The ruthenium content was measured using an inductively coupled plasma optical emission spectrometer (ICP-OES, Agilent ICP-OES 720).

The average particle size of Ru nanoparticles in the sample was determined using the Scherrer formula:

$$D = K\lambda/(\beta\cos\theta) \qquad \text{Formula S1}$$

Among these variables, K is the Scherrer constant, typically valued at 0.89; D represents the average grain size (in Å); B is the full width at half maximum (FWHM) of the measured diffraction peak, which must be converted to radians; θ is the Bragg diffraction angle, equal to half of 2θ, and also needs to be converted to radians for calculating the cosine value; γ is the X-ray wavelength, which for Cu Kα radiation is generally 1.54056 Å.

3. Electrochemical Tests

The alkaline hydrogen evolution reaction (HER) activity was tested using a three-electrode electrolytic cell, with a 1 M KOH solution as the electrolyte. A catalyst-coated glassy carbon electrode (GCE) served as the working electrode, with a platinum (Pt) wire as the counter electrode and Hg/HgO as the reference electrode. 2 mg of catalyst was dispersed in 200 μL of a mixed solvent containing isopropyl alcohol and 5% Nafion under sonication. Then, 5 μL of the resulting ink was deposited onto the surface of the GCE. All catalysts were activated by performing 20 cycles of cyclic voltammetry (CV) prior to electrochemical testing. To evaluate the activity of each electrocatalyst, linear sweep voltammetry (LSV) was conducted at a scan rate of 5 mV s^{-1}.

All measured potentials in this study are referenced to a reversible hydrogen electrode (RHE) and converted according to the following equation:

$$E_{(RHE)} = E_{(Hg/HgO)} + 0.0591 \times pH + 0.098\ V \qquad \text{Formula S2}$$

Using **Formula S2** below, fit the linear portion of the LSV curve to determine the

Tafel slope.

$\eta = a + b \times \log|j|$ Formula S3

Where η is the overpotential, b is the Tafel slope, and j represents the current density.

According to **Formula S3**, the electrochemically active surface area (ECSA) is calculated using the following equation:

$ECSA = (C_{dl} \times S) / C_s$ Formula S4

Where C_{dl} is the double-layer capacitance, S is the area of the working electrode, and C_s (0.04 mF cm^{-2}) is the specific capacitance of the sample. The value of C_{dl} is measured by cyclic voltammetry at different scan rates ranging from 20 mV s^{-1} to 120 mV s^{-1}.

4. DFT calculation method

All density functional theory (DFT) calculations were carried out using the Vienna Ab Initio Simulation Package (VASP). The generalized gradient approximation (GGA) with the Perdew–Burke–Ernzerhof (PBE) functional was employed to describe the exchange–correlation interactions. The projector augmented wave (PAW) method was used to treat the ion–electron interactions, and valence electrons were expanded using a plane-wave basis set with a kinetic energy cutoff of 450 eV. Partial occupancies of the Kohn–Sham orbitals were treated using the Gaussian smearing method with a smearing width of 0.05 eV. The electronic self-consistent calculations were considered converged when the total energy change was smaller than 1×10^{-5} eV. Geometry optimizations were regarded as converged when the residual forces on each atom were less than 0.03 eV $Å^{-1}$. Grimme's DFT-D3 method was employed to account for long-range dispersion interactions. Surface models of Ru and RuO_2 were constructed using periodic slab geometries. A vacuum layer of 20 Å was applied perpendicular to the surface to avoid interactions between periodic images. The Brillouin zone integration was performed using a Monkhorst–Pack k-point mesh of 2 × 2 × 1 for surface calculations.

The charge density difference was calculated according to:

$\Delta\rho = \rho\_total - \rho\_surface - \rho\_H$ Formula S5

where ρ_total is the charge density of the adsorption system, and ρ_surface and ρ_H correspond to the charge densities of the clean Ru or RuO_2 surface and the adsorbed hydrogen species, respectively.

The adsorption energy of hydrogen (E_ads) was calculated using the following expression:

$$\Delta E_{ads} = E_{adsorbate/slab} - E_{slab} - E_{adsorbate} \quad \text{Formula S6}$$

where E_adsorbate/slab is the total energy of the adsorbate–surface system, E_slab is the total energy of the clean catalyst surface, and E_adsorbate is the total energy of the isolated adsorbate in the gas phase.

The Gibbs free energy of hydrogen adsorption (ΔG_H) for the hydrogen evolution reaction (HER) was calculated according to:

$$\Delta G_H = \Delta E_{ads} + \Delta E_{ZPE} - T\Delta S \quad \text{Formula S7}$$

where ΔE_ads is the hydrogen adsorption energy obtained from DFT calculations, ΔE_ZPE is the zero-point energy correction, and ΔS is the entropy change. The entropy contribution of adsorbed hydrogen was assumed to be negligible, while the entropy of hydrogen in the gas phase was taken from standard thermodynamic data.

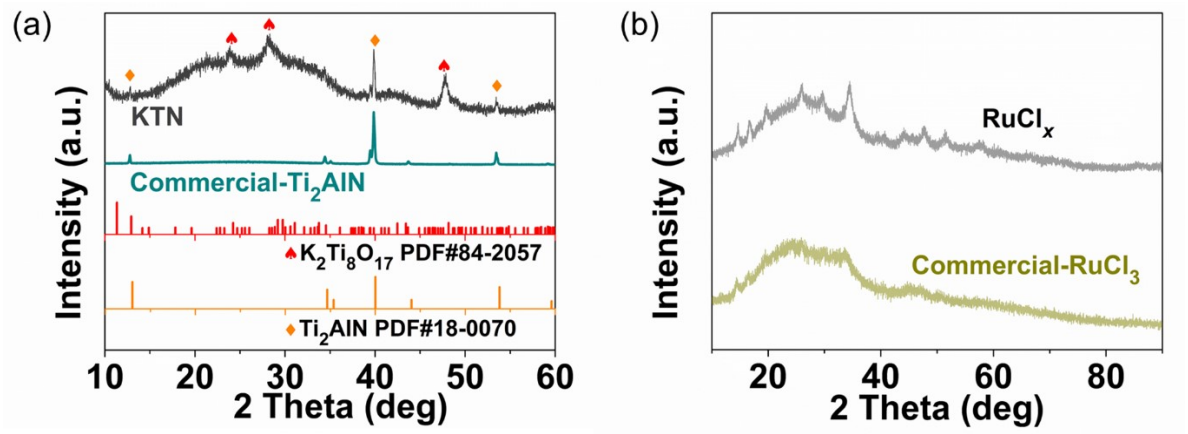

Figure S1. (a) XRD patterns of KTN and commercial Ti_2AlN. (b) XRD patterns of $RuCl_x$ and commercial $RuCl_3$.

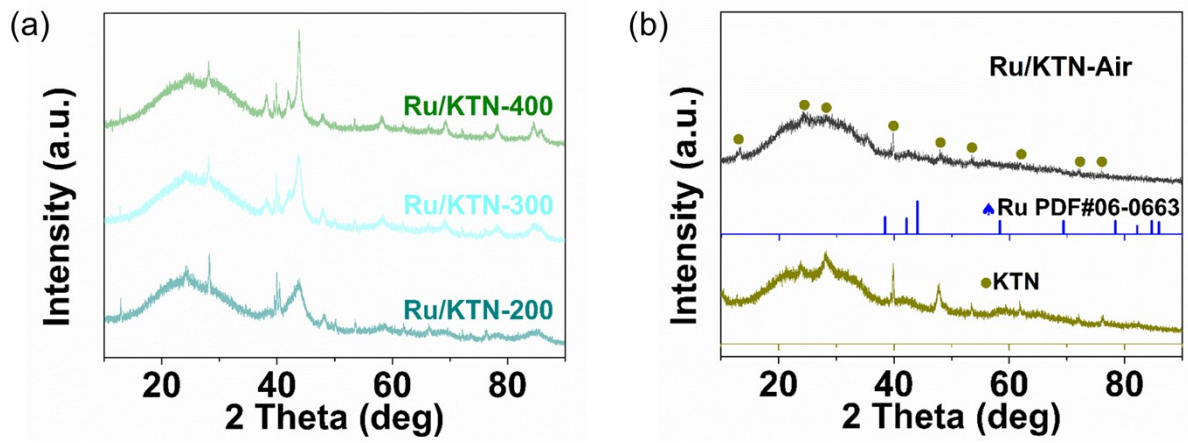

Figure S2. (a) XRD patterns of Ru/KTN-200, Ru/KTN-300, and Ru/KTN-400. (b) XRD patterns of Ru/KTN-Air.

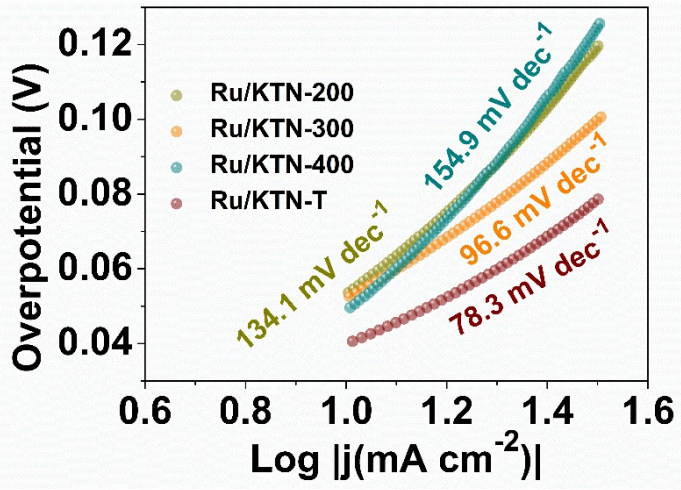

Figure S3. Tafel slopes at high current densities.

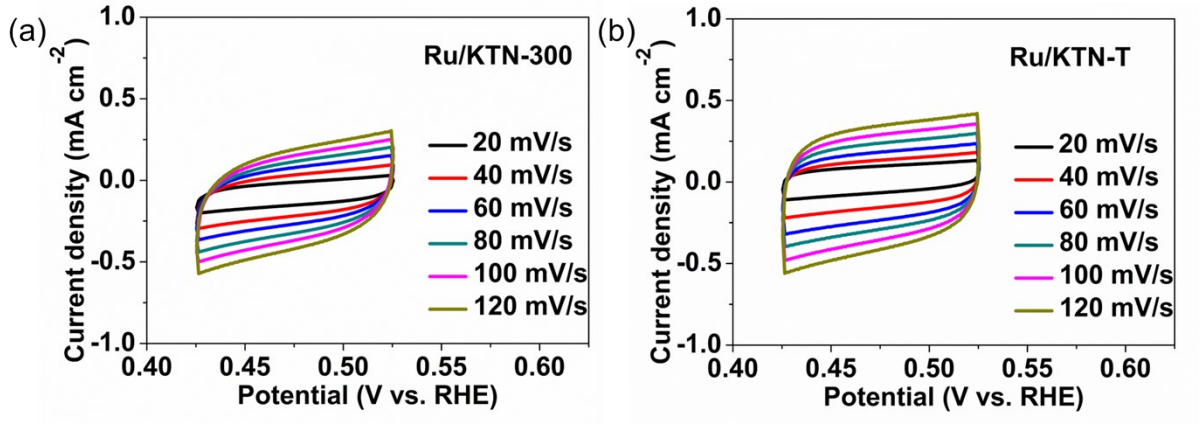

Figure S4. Cyclic voltammetry curves of (a) Ru/KTN-300, (b) Ru/KTN-T.

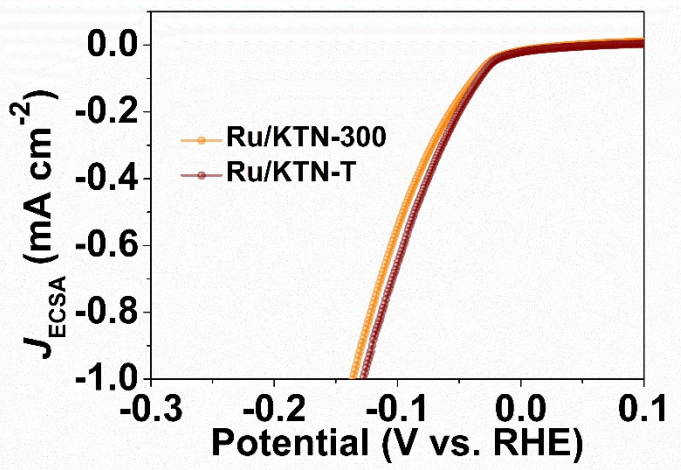

Figure S5. LSV curves normalized by ECSA.

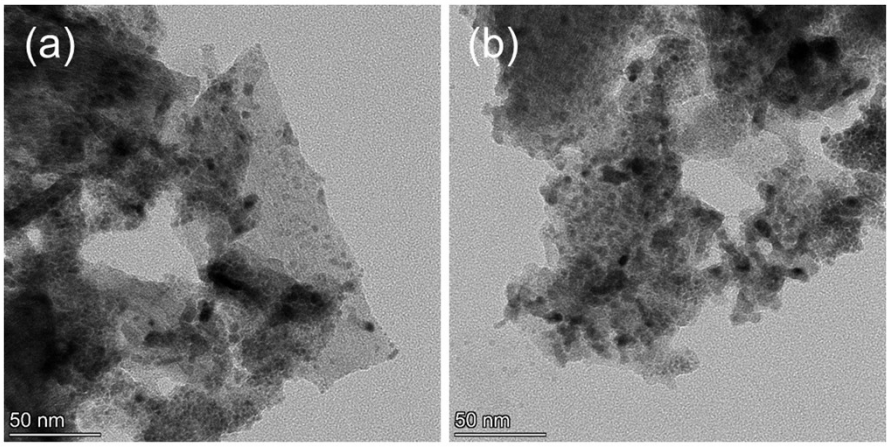

Figure. S6 TEM images of Ru/KTN-T before (a) and after (b) the 100-hour stability test.

Table S1. The average size of the sample Ru particles calculated using the Scherrer formula.

Sample	Crystal plane	Angle (2θ, °)	FWHM (°)	Particle size (nm)
Ru/KTN-300	(101)	43.91	0.764	11.09
Ru/KTN-T	(101)	43.74	0.692	12.23

Table S2. Summary of some Ru-based supported electrocatalysts.

Electrocatalyst	Electrolyte	Overpotential (mV, η_{10})	Tafel slope (mV/dec)	Ref.
m-Ru@TiO_{2-x}	1 M KOH	47	51.0	1
Ru/C-TiO_2	1 M KOH	44	73.7	2
Ru/P-TiO_2	1 M KOH	27	28.3	3
Ru@TiO_2	0.1 M KOH	57	67	4
Ru-TiO/TiO_2@NC	1 M KOH	39	49	5
R-TiO_2:Ru 5%	0.1 M KOH	150	95	6
Ru-Mo_2C@CNT	1 M KOH	15	26	7
Ru@1T-MoS_2-MXene	1 M KOH	42	38	8
SA-Ru-MoS_2	1 M KOH	76	21	9
Ru_1@D-MoS_2	1 M KOH	107	96	10
Ru-MoS_2/CC	1 M KOH	41	114	11
Ru/ZC-E50	1 M KOH	29	82	12
Ru-Ru_2P/PC-2	1 M KOH	43.4	35.1	13
RuP_2@NPC	1 M KOH	52	69	14
Ru/TKN-T	1 M KOH	40.6	40	This work
Commercial Pt/C	1 M KOH	33.6	/	This work
Commercial Ru/C	1 M KOH	46.6	/	This work

References

1 F. T. Li, N. N. Cui, Y. N. Zhou, S. Q. Sun, C. L. Li, Z. K. Wang and S. Q. Hu, *Journal of Alloys and Compounds*, 2025, **1010**, 177239.

2 Y. J. Wang, Q. X. Zhu, T. P. Xie, Y. Peng, S. L. Liu and J. K. Wang, *Chemelectrochem*, 2020, **7**, 1182-1186.

3 S. Zhou, H. Jang, Q. Qin, L. Hou, M. G. Kim, S. Liu, X. Liu and J. Cho, *Angewandte Chemie International Edition*, 2022, **134**, e202212196.

4 S. Liang, C. L. Dong, C. Zhou, R. Q. Wang and F. Q. Huang, *Nano Letters*, 2024, **24**, 757-763.

5 L. Jing, G. Jie, W. Q. Yu, H. W. Ren, X. J. Cui, X. Chen and L. H. Jiang, *Chemical Engineering Journal*, 2023, **472**, 145009.

6 S. Y. Nong, W. J. Dong, J. W. Yin, B. W. Dong, Y. Lu, X. T. Yuan, X. Wang, K. J. Bu, M. Y. Chen, S. D. Jiang, L. M. Liu, M. L. Sui and F. Q. Huang, *Journal of the American Chemical Society*, 2018, **140**, 5719-5727.

7 X. K. Wu, Z. C. Wang, D. Zhang, Y. N. Qin, M. H. Wang, Y. Han, T. R. Zhan, B. Yang, S. X. Li, J. P. Lai and L. Wang, *Nature Communications*, 2021, **12**, 4018.

8 G. Z. Li, T. Sun, H. J. Niu, Y. Yan, T. Liu, S. S. Jiang, Q. L. Yang, W. Zhou and L. Guo, *Advanced Functional Materials*, 2023, **33**, 2212514.

9 J. M. Zhang, X. P. Xu, L. Yang, D. J. Cheng and D. P. Cao, *Small Methods*, 2019, **3**, 1900653.

10 C. Lang, W. Jiang, C. J. Yang, H. Zhong, P. Chen, Q. Wu, X. Yan, C. L. Dong, Y. Lin, L. Ouyang, Y. Jia and X. Yao, *Small*, 2023, **19**, 2300807.

11 D. W. Wang, Q. Li, C. Han, Z. C. Xing and X. R. Yang, *Applied Catalysis B-Environment and Energy*, 2019, **249**, 91-97.

12 Y. J. Jiang, T. W. Huang, H. L. Chou, L. H. Zhou, S. W. Lee, K. W. Wang and S. Dai, *Journal of Materials Chemistry A*, 2022, **10**, 17730-17739.

13 Z. Liu, Z. Li, J. Li, J. Xiong, S. F. Zhou, J. W. Liang, W. W. Cai, C. W. Wang, Z. H. Yang and H. S. Cheng, *Journal of Materials Chemistry A*, 2019, **7**, 5621-5625.

14 Z. H. Pu, I. S. Amiinu, Z. K. Kou, W. Q. Li and S. C. Mu, *Angewandte Chemie-International Edition*, 2017, **56**, 11559-11564.